



ELSEVIER



CrossMark



# A Time-Split Discontinuous Galerkin Transport Scheme for Global Atmospheric Model

Ram D. Nair<sup>1</sup>, Lei Bao<sup>2</sup>, and Michael D. Toy<sup>3</sup>

<sup>1</sup> National Center for Atmospheric Research\*,  
Boulder, CO 80305, USA

[rnair@ucar.edu](mailto:rnair@ucar.edu)

<sup>2</sup> Dept. of Applied Mathematics,  
University of Colorado, Boulder, CO, USA

[leibao@colorado.edu](mailto:leibao@colorado.edu)

<sup>3</sup> National Center for Atmospheric Research,  
Boulder, CO 80305, USA

[toy@ucar.edu](mailto:toy@ucar.edu)

## Abstract

A time-split transport scheme has been developed for the high-order multiscale atmospheric model (HOMAM). The spacial discretization of HOMAM is based on the discontinuous Galerkin method, combining the 2D horizontal elements on the cubed-sphere surface and 1D vertical elements in a terrain-following height-based coordinate. The accuracy of the time-splitting scheme is tested with a set of new benchmark 3D advection problems. The split time-integrators are based on the Strang-type operator-split method. The convergence of standard error norms shows a second-order accuracy with the smooth scalar field, irrespective of a particular time-integrator. The results with the split scheme is comparable with that of the established models.

*Keywords:* Cubed sphere, discontinuous Galerkin, transport scheme, time-split scheme

## 1 Introduction

Global nonhydrostatic (NH) models with horizontal grid resolutions on the order of a few kilometers are becoming increasingly popular due to the recent paradigm shift in supercomputing resources. Many climate modeling groups have already begun to develop NH models [17, 19]. The High-Order Method Modeling Environment (HOMME), developed at NCAR, is a petascale hydrostatic framework, which employs the cubed-sphere grid system and high-order Galerkin methods. The spatial discretization is based on both the spectral-element (SE) and discontinuous Galerkin (DG) methods [12], and the time integration is based on explicit methods. The

\*The National Center for Atmospheric Research is sponsored by the National Science Foundation.

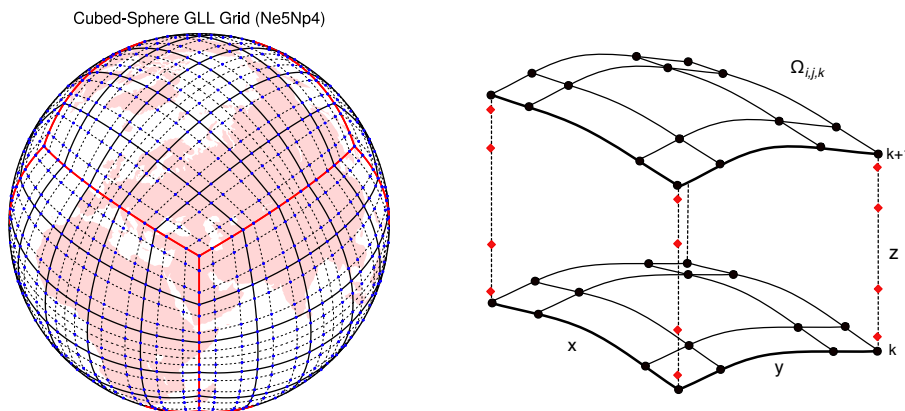


Figure 1: Schematic diagram showing the horizontal and vertical grid structure for HOMAM. The horizontal grid system relies on a cubed-sphere (left panel) tiled with GLL quadrature elements and stacked in the vertical (radial) direction. The vertical grid lines comprise 1D elements with GL quadrature points as shown in the right panel.

SE variant of HOMME is used as the default hydrostatic dynamical core (CAM-SE [5, 8]) for NCAR’s community atmospheric model.

Recently, the HOMME framework is being extended to a NH dynamical core, the “High-Order Multiscale Atmospheric Model (HOMAM)”. Since the DG method possesses computationally desirable properties such as local and global conservation, geometric flexibility, high on-processor operations and minimal communication footprints, it is used as the basic spatial discretization scheme for the HOMAM. Orography is handled by the terrain-following height-based coordinate system. Traditionally, 3D global NH models are developed in a dimension-split manner, which combines the horizontal 2D (spherical surface) and vertical 1D domains, using various standard discretization techniques [16, 15, 19]. A major reason for this is the ease of implementing various semi-implicit time integration schemes, which alleviates the stringent CFL stability requirement resulting from the vertical aspects of the dynamics. Although the DG method can handle 3D elements [2, 10], we prefer to use the conventional dimension-split approach for HOMAM because of the previously stated reason.

One of the major challenges for NH modeling is to develop a practical time-stepping method. The high aspect ratio between horizontal and vertical grid spacing combined with fast-moving acoustic waves impose a stringent stability constraint for explicit time stepping. A recent study [1] introduces a time-splitting approach that is horizontally-explicit and vertically-implicit (HEVI) and relies on the Strang-type operator-split philosophy as a practical way to address this problem for high-order DG NH models [1]. The model time stepping is independent of the vertical resolution, and is limited only by the horizontal Courant number. Our goal is to extend the HEVI scheme to the HOMAM framework for practical NH dynamics, and testing the 3D transport scheme is a step toward this direction.

In HOMAM we test the HEVI scheme and the horizontally-explicit, vertically-explicit (HEVE) scheme, and their performance is compared against a fully explicit Runge-Kutta method without time-splitting. The Dynamical Core Model Intercomparison Project (DCMIP) [9], provides a set of benchmark test cases for validating global NH atmospheric models. Recently, Kent et al. [11] used a subset of DCMIP tests specifically designed for 3D global advective

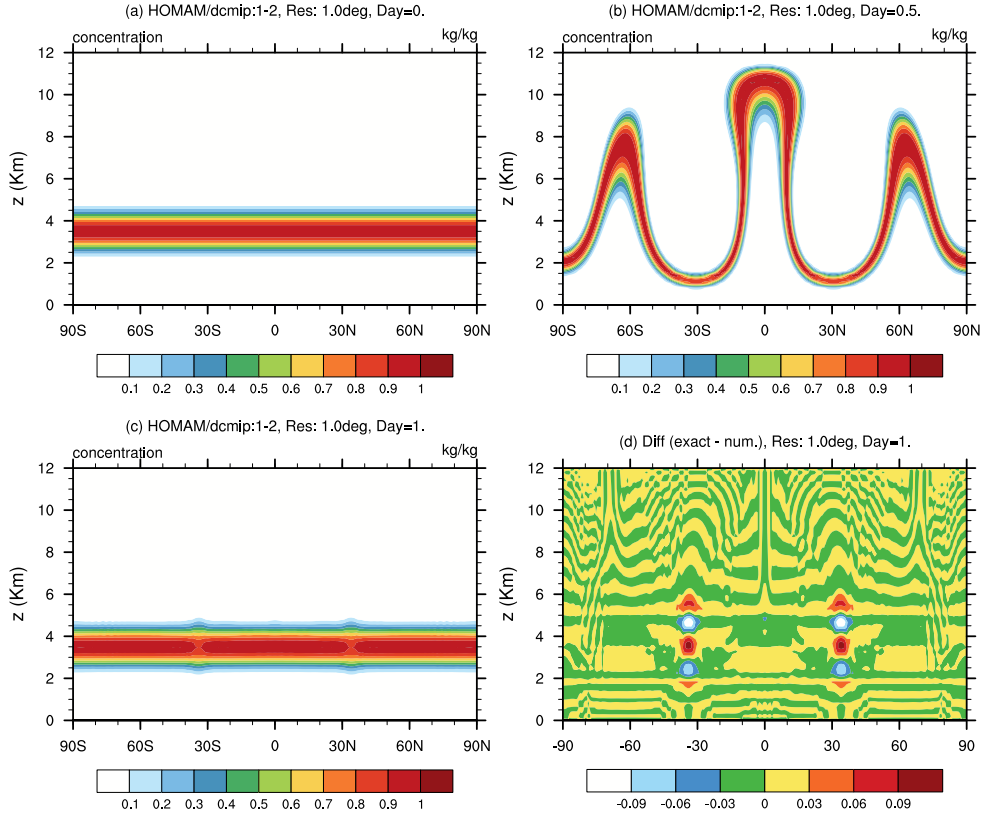


Figure 2: Vertical meridional cross-section of the tracer field  $q = q_1$  for the Hadley test (DCMIP 1-2), simulated with HOMAM at a horizontal resolution of  $1^\circ \times 1^\circ$  ( $N_e = 30, N_p = 4, N_g = 4$ ) with 60 vertical levels and  $\Delta t = 60$ s at times (a)  $t = 0$ , (b)  $t = 12$ , and (c)  $t = 24$  hours. The difference between the analytical and simulated field at  $t = 24$  hours is shown in (d).

tion, and compared the performance of different atmospheric models. For the current study, we are particularly interested in two challenging advection test-cases to validate the time-split transport scheme used in HOMAM.

## 2 The 3D advection scheme

The transport equation for a passive tracer with mixing ratio  $q$ , without sources or sinks, can be written in the following conservative flux form:

$$\frac{\partial \rho q}{\partial t} + \nabla \cdot (\vec{v} \rho q) = 0, \quad (1)$$

where  $\rho$  is the air density,  $\vec{v}$  is the wind field and  $\nabla$  is the gradient operator in 3D. Note that  $\rho$  follows the mass continuity equation  $\partial \rho / \partial t + \nabla \cdot (\vec{v} \rho) = 0$ . In order to simplify the test criteria, [11] used a divergence-free field  $\vec{v} \rho$ , and the resulting time-independent density  $\rho$  is analytically prescribed as an initial condition.

## 2.1 Computational domain

The horizontal domain for HOMAM is a sphere  $\mathcal{S}$  representing the planet Earth, and is based on the cubed-sphere topology shown in Fig. 1. To formulate the transport equation in the 3D framework, we first consider the horizontal aspects in  $(x^1, x^2)$  computational coordinates, which forms the surface of a logical cube. Here we consider the cubed-sphere geometry employing the equiangular central projection as described in Nair et al. [14]. Each of the local coordinate systems is free of singularities, employs identical metric terms, and creates a non-orthogonal curvilinear coordinate system for  $\mathcal{S}$ . The local coordinates (or central angles of the projection) for each face are  $x^1 = x^1(\lambda, \phi)$ ,  $x^2 = x^2(\lambda, \phi)$  such that  $x^1, x^2 \in [-\pi/4, \pi/4]$ , where  $\lambda$  and  $\phi$  are the longitude and latitude, respectively, of a sphere with radius  $r$ . The second-order metric tensor  $G_{ij}$  associated with the central projection is

$$G_{ij} = \frac{r^2}{\mu^4 \cos^2 x^1 \cos^2 x^2} \begin{bmatrix} 1 + \tan^2 x^1 & -\tan x^1 \tan x^2 \\ -\tan x^1 \tan x^2 & 1 + \tan^2 x^2 \end{bmatrix}, \quad (2)$$

where  $i, j \in \{1, 2\}$  and  $\mu^2 = 1 + \tan^2 x^1 + \tan^2 x^2$ .

The orthogonal components of the spherical wind vector  $\mathbf{v}(\lambda, \phi) = (u, v)$  can be expressed in terms of contravariant vectors  $(u^1, u^2)$  as follows:

$$\begin{bmatrix} u \\ v \end{bmatrix} = \mathbf{A} \begin{bmatrix} u^1 \\ u^2 \end{bmatrix}, \quad \mathbf{A}^T \mathbf{A} = G_{ij}. \quad (3)$$

The Jacobian of the transformation (the metric term) is  $\sqrt{G_h} = [\det(G_{ij})]^{1/2} = |\mathbf{A}|$ . The details of the local transformation laws and  $\mathbf{A}$  for each face of the cubed-sphere can be found in [14].

The transport equation can be generally expressed in 3D  $(x^1, x^2, x^3)$  curvilinear coordinates, where  $x^3$  denotes the variable in the radial (vertical) direction  $\vec{r}$  with respect to the sphere. With the shallow atmosphere approximation,  $r$  is treated as a constant such that  $x^3 = r + z$  and  $z \ll r$ , where  $z$  may be interpreted as the geometrical height from the surface. Thus the independent variables are  $(x^1, x^2, z)$  in the computational coordinates, and the vertical velocity is given by  $w = dz/dt$ . Note that the horizontal metric term  $\sqrt{G_h}$  is independent of  $z$ . The transport equation (1) in flux-form for a tracer variable  $q$  in 3D  $(x^1, x^2, z)$  coordinates can be written as

$$\frac{\partial \rho q}{\partial t} + \frac{1}{\sqrt{G_h}} \left[ \frac{\partial}{\partial x^1} (\sqrt{G_h} \rho q u^1) + \frac{\partial}{\partial x^2} (\sqrt{G_h} \rho q u^2) + \frac{\partial}{\partial z} (\sqrt{G_h} \rho q w) \right] = 0. \quad (4)$$

The accurate representation of terrain is very important for practical NH modeling where mountain waves are forced by the irregularities of the earth's surface. Although the DG method is capable of handling complex terrain with an unstructured grid, we prefer to use the classical terrain-following coordinates introduced by Gal-Chen and Sommerville [6] for Eq. (4). In order to introduce the height-based terrain-following coordinates, the  $(x^1, x^2, z)$  system is transformed into  $(x^1, x^2, \zeta)$  coordinates [6]. Let  $h_s = h_s(x^1, x^2)$  be the prescribed mountain profile and  $z_{top}$  is the top of the model domain, then the vertical  $z$  height coordinate can be transformed to the monotonic  $\zeta$  coordinate using the following mapping:

$$\zeta = z_{top} \frac{z - h_s}{z_{top} - h_s}, \quad z(\zeta) = h_s(x^1, x^2) + \zeta \frac{z_{top} - h_s}{z_{top}}; \quad h_s \leq z \leq z_{top}. \quad (5)$$

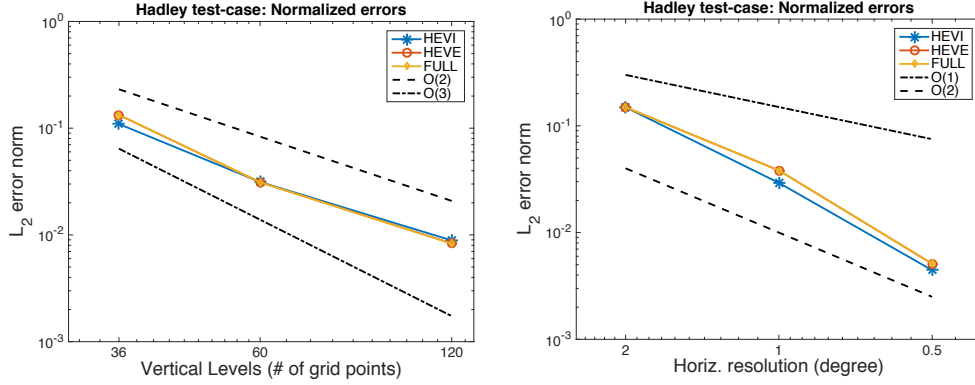


Figure 3: Convergence of  $\ell_2$  error norm for the Hadley test after 1 day with HOMAM. The left panel shows the explicit un-split RK (FULL), HEVE and HEVI schemes at a fixed horizontal resolution of  $1^\circ$ ,  $\Delta t = 6s$ , and varying vertical levels. The right panel shows results of varying the 3D (horizontal and vertical) resolution.

The Jacobian associated with the vertical transform in  $(x, y, z) \rightarrow (x^1, x^2, \zeta)$  is

$$\sqrt{G_v} = \left[ \frac{\partial z}{\partial \zeta} \right]_{(x^1, x^2)} = 1 - \frac{h_s(x^1, x^2)}{z_{top}}. \quad (6)$$

The vertical velocity in the  $\zeta$ -coordinate is  $\tilde{w} = d\zeta/dt$  and is related to  $w$  via [3]

$$\sqrt{G_v} \tilde{w} = w + \sqrt{G_v} G_v^{13} u^1 + \sqrt{G_v} G_v^{23} u^2, \quad (7)$$

where the metric coefficients are defined as follows:

$$\sqrt{G_v} G_v^{13} = \left[ \frac{\partial h_s}{\partial x^1} \right]_{(z)} \left( \frac{\zeta}{z_{top}} - 1 \right), \quad \sqrt{G_v} G_v^{23} = \left[ \frac{\partial h_s}{\partial x^2} \right]_{(z)} \left( \frac{\zeta}{z_{top}} - 1 \right),$$

where the horizontal derivatives of the surface topography are analytically determined for the DCMIP test cases to follow. The final form of (4) can be written in the  $(x^1, x^2, \zeta)$  coordinates as follows,

$$\frac{\partial \psi}{\partial t} + \frac{\partial(\psi u^1)}{\partial x^1} + \frac{\partial(\psi u^2)}{\partial x^2} = -\frac{\partial(\psi \tilde{w})}{\partial \zeta}, \quad (8)$$

where the pseudo density  $\psi = \sqrt{G_h} \sqrt{G_v} \rho q$ , combines the time-independent horizontal ( $\sqrt{G_h}$ ) and the vertical ( $\sqrt{G_v}$ ) metric terms, and the conservative variable  $\rho q$ .

## 2.2 Nodal DG discretization

The computational domain  $\mathcal{D}$  corresponding to  $\mathcal{S}$  is the surface of a logical cube, which consists of  $N_e \times N_e \times 6$  elements, where  $N_e$  is the number of elements in each of the  $x^1$  and  $x^2$  directions. Figure 1 shows a cubed-sphere  $\mathcal{S}$  (left panel) tiled with elements. Transport equation (8) can be written in the following generalized form as a conservation law,

$$\frac{\partial U}{\partial t} + \nabla \cdot \mathbf{F}(U) = S(U) \quad \text{in } \mathcal{D} \times (0, T], \quad (9)$$

where  $U = \psi$ ,  $\mathbf{F} = (\psi u^1, \psi u^2)$ ,  $\nabla = (\partial/\partial x^1, \partial/\partial x^2)$  and  $T$  is a prescribed time. The source term  $S(U)$  appearing in (9) corresponds to the vertical derivative on the RHS of (8). Without loss of generality, we may describe the DG discretization on a horizontal layer (cubed-sphere surface), defined by  $\zeta = \zeta_k$  of the 3D domain. Let  $\mathcal{V}_h$  be a vector space of polynomials of degree up to  $N$  such that the approximate solution  $U_h \approx U$  belongs to  $\mathcal{V}_h$ . Let  $\Omega_{ij}$  be a generic element in  $\mathcal{D}$  with the boundary  $\Gamma_{ij}$ . The weak Galerkin formulation of the problem can be obtained by multiplying (9) by the test function  $\varphi_h \in \mathcal{V}_h$ , and integrating by parts over  $\Omega_{ij}$  [4]:

$$\frac{d}{dt} \int_{\Omega_{ij}} U_h \varphi_h d\Omega - \int_{\Omega_{ij}} \mathbf{F}(U_h) \cdot \nabla \varphi_h d\Omega + \int_{\Gamma_{ij}} \widehat{\mathbf{F}} \cdot \mathbf{n} \varphi_h d\Gamma = \int_{\Omega_{ij}} S(U_h) \varphi_h d\Omega, \quad \forall \Omega_{ij} \in \mathcal{D}, \quad (10)$$

where  $\mathbf{n}$  is the outward-drawn unit normal vector on  $\Gamma_{ij}$ , and  $\widehat{\mathbf{F}}$  is the local Lax-Friedrichs numerical flux [4, 13].

In order to evaluate the integrals in (10) efficiently, the element  $\Omega_{ij}$  is first mapped onto the standard element  $[-1, 1]^2$ , and then the Gauss-Lobatto-Legendre (GLL) or Gauss-Legendre (GL) quadrature rules are employed. Here we adopt the nodal DG discretization which employs the Lagrange polynomials  $h_l(\xi)$ ,  $\xi \in [-1, 1]$ ,  $0 \leq l \leq N$  (with  $N + 1 = N_p$  solution points), as the basis functions with roots at the GLL quadrature points (see [13] for details). This is the standard setup in the HOMME framework which we adopt in our current work.

In a dimension-split case, the source term  $S(U)$  appearing in (9) corresponds to the vertical derivative on the RHS of (8). However, here we consider DG spatial discretization analogous to (10) for  $K$  vertical 1D elements in  $[h_s, z_{top}]$ , in which we employ the GL quadrature grid (see Fig. 1 right panel). The GL quadrature is more accurate than the GLL case and allows  $K \times N_g$  independent vertical levels, where  $N_g$  is the number of GL points. Thus the total degrees-of-freedom for the time-evolving global tracer field  $q$  is  $6 N_e^2 N_p^2 \times K N_g$ . The semi-discretized equation corresponding to (10) can generally be written in the following form:

$$\frac{d}{dt} U = L(U) \quad \text{in} \quad (0, T), \quad (11)$$

where  $L$  indicates DG spatial discretization.

### 2.3 Time integration

We consider three time integrators for solving (11): an explicit Runge-Kutta (RK) method and the time-split schemes HEVE and HEVI. The RK method we consider is the third-order strong stability-preserving RK [7] scheme, hereafter referred to as the un-split RK3 scheme.

Letting  $U^n = U_h(t)$  and  $U^{n+1} = U(t + \Delta t)$ , the three-stage un-split RK3 time integration scheme can be written in the following manner:

$$\begin{aligned} U^{(1)} &= U^n + \Delta t L(U^n) \\ U^{(2)} &= \frac{3}{4} U^n + \frac{1}{4} U^{(1)} + \frac{1}{4} \Delta t L(U^{(1)}) \\ U^{n+1} &= \frac{1}{3} U^n + \frac{2}{3} U^{(2)} + \frac{2}{3} \Delta t L(U^{(2)}). \end{aligned} \quad (12)$$

The HEVE scheme has only a limited practical value for NH models, nevertheless, it gives reference results for comparison with the HEVI scheme. The HEVE scheme is based on the Strang operator-split approach [1], which is up to  $O(\Delta t^2)$  accurate. The spatial DG discretization  $L(U)$  corresponding to (8) is decomposed into the horizontal  $L^H$  and vertical  $L^V$  parts

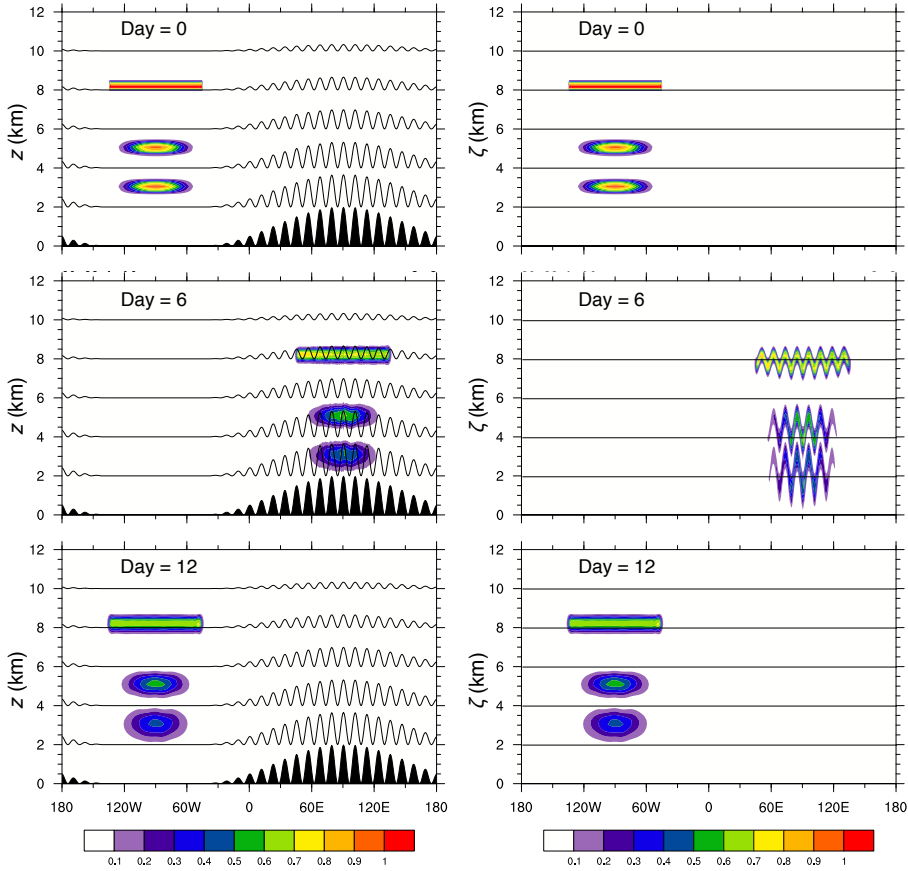


Figure 4: Vertical cross-sections along the equator for the tracer field  $q = q_4$  for the DCMIP test 1-3 with the top panels showing the initial fields. Left and right columns show the simulated results on the vertical  $z$  and transformed  $\zeta$  coordinates, respectively, at days 6 and 12. The black shading indicates  $z$  bottom topography and the dark thin lines are reference horizontal grid lines. The results are simulated with HOMAM using the HEVE scheme at a horizontal resolution of  $1^\circ$ , 60 vertical levels, and  $\Delta t = 12\text{s}$ .

such that  $L(U) = L^H(U) + L^V(U)$ . For the given time interval  $[t, t + \Delta t]$ , the Strang-splitting scheme has the following 3 steps:

$$U_1 := U_h(t), \quad \frac{d}{dt}U_1 = L^H(U_1) \quad \text{in } (t, t + \Delta t/2] \quad (13)$$

$$U_2 := U_1(t + \Delta t/2), \quad \frac{d}{dt}U_2 = L^V(U_2) \quad \text{in } (t, t + \Delta t], \quad (14)$$

$$U_3 := U_2(t + \Delta t), \quad \frac{d}{dt}U_3 = L^H(U_3) \quad \text{in } (t + \Delta t/2, t + \Delta t], \quad (15)$$

and  $U_h(t + \Delta t) = U_3(t + \Delta t)$ . The above HEVE algorithm follows an  $H - V - H$  cycle, and each stage requires an ODE solve, which can be performed with (12). However, for the HEVI scheme the second stage (15) is replaced with a 1D vertical implicit solver by using the DIRK (diagonally implicit RK) method as used in [1]. For brevity we exclude the details.

### 3 Numerical Experiments

The DCMIP [9] test suite includes benchmark advection test cases for global transport problems, where a 3D non-divergent wind field is prescribed. The details of the test configurations and standard error norms are well documented in [11], which we do not describe herein. The initial conditions include prescribed functions for the tracer field  $q$ , density  $\rho$  and the 3D analytical velocity field  $(u, v, w)$ . The wind fields are converted to computational coordinates  $(x^1, x^2, \zeta)$ , consistent with HOMAM, using the relations (3) and (7). For the test-cases considered herein, we use  $4 \times 4$  GLL points for horizontal elements ( $N_p = 4$ ) and  $N_g = 4$  GL points in the vertical 1D elements. No limiter or filter is used with the advection scheme.

Errors/Models:	Mcore	CAM-FV	CAM-SE	HOMAM
$l_1$	2.22	1.93	2.27	2.62
$l_2$	1.94	1.84	2.12	2.43
$l_\infty$	1.64	1.66	1.68	2.16

Table 1: Average convergence rate for the normalized error norms for the Hadley test (DCMIP test 1-2) computed using resolutions  $2^\circ, 1^\circ, 0.5^\circ$  horizontal, and respectively with 30, 60, 120 vertical levels, and with  $\Delta t = 6$ s for HOMAM.

Error/Levels:	L36	L60	L120
$l_1$	1.3534	0.9654	0.7841
$l_2$	0.7541	0.5458	0.4989
$l_\infty$	0.8864	0.7655	0.7658

Table 2: Error norms at different vertical resolutions with a fixed horizontal resolution  $1^\circ$  and  $\Delta t = 12$ s for the DCMIP test 1-3.

#### 3.1 Meridional ‘‘Hadley’’ circulation

This experiment is test case 1-2 of the DCMIP test suite [9, 11], in which a deformational flow that mimics a Hadley-like meridional circulation is prescribed. The initial scalar field  $q$  is a quasi-smooth cosine profile. The wind fields are designed so that the flow reverses itself halfway through the simulation and returns the tracers to their initial position, therefore, the exact solution is known at the end of the run. This test is designed to investigate the impact of horizontal-vertical spatial splitting on the accuracy of the scheme.

Figure 2 shows a vertical-meridional slice of the tracer field along the  $180^\circ$  longitude line at four different times during the 1-day simulation with the HOMAM. The horizontal resolution is  $1^\circ \times 1^\circ$  ( $N_e = 30, N_p = 4, N_g = 4$ ), there are 60 vertical levels, and the time step is 60 seconds. At  $t = 12$  hours, the tracer field is at its maximum displacement from the initial condition. At the end of the simulation ( $t = 24$  hours), the tracer field closely resembles its initial value, with some deviation noticeable near latitudes  $\pm 30^\circ$  where the tracer field experienced the most stretching. The resolution dependency of the normalized errors at a fixed small time step of 6 seconds is shown in Fig. 3. The left-hand panel indicates that the vertical convergence rate is approximately 2nd-order, while the right-hand panel shows a combined horizontal-vertical convergence rate of greater than 2nd-order. Table 1 compares the combined horizontal and vertical convergence rates of four different models, including Mcore[18], CAM-FV [11] and CAM-SE [8], for the Hadley experiment. The HOMAM has the highest rate of convergence of the models. Figure 3 also shows that the split time differencing schemes (both HEVE and HEVI) have a minimal effect on the error norms when compared to the explicit un-split RK3

scheme. The results of temporal convergence tests (not shown) indicate between first- and second-order convergence with the split schemes for the Hadley simulation. However, this test is not ideal for studying time-discretization errors. Solid-body rotation would be better suited for this purpose and the model will be tested with this case in the future. Also, the effects of stability with the Strang splitting on the horizontally explicit component will also be tested.

### 3.2 Advection over rough topography

DCMIP test-case 1-3 [9] investigates the ability of the tracer transport algorithm to accurately advect tracers over topography. A series of steep concentric ring-shaped mountain ranges forms the terrain. The prescribed flow field is a constant solid-body rotation and the tracer field  $q$  is given by three thin vertically stacked cloud-like patches (non-smooth) which circumnavigate the globe and return to their initial positions after 12 days. In height coordinates, the vertical velocity ( $w$ ) is zero, however, in the terrain-following vertical  $\zeta$  coordinate system, there is a vertical velocity ( $\tilde{w}$ ) caused by the topography which induces cross-coordinate vertical advection. As in DCMIP test-case 1-2, the exact solution at the end of the run is the initial condition.

Figure 4 shows the results of the simulation with HOMAM at the initial condition, halfway into the simulation when the tracer fields are centered over the highest mountains, and at the end of the run when the tracers have returned to their original position. Overall, the shapes of the tracer patches have been maintained, however, some dissipation has occurred. The right-hand column of panels in Fig. 4 shows the tracer fields in the model coordinate ( $\zeta$ ) system. The plot at day 6 shows the considerable vertical displacement across model levels that occurs. Table 2 shows the normalized errors for the runs with varying vertical resolution and the horizontal resolution fixed at  $1^\circ$  and the time step at 12 seconds. The error norms of HOMAM are comparable to or better than those of other models presented in [11]. As in the Hadley experiment, the split-explicit (HEVE) time-stepping scheme has almost no effect on the errors (results not shown).

## 4 Summary

Various time stepping schemes were tested for 3D advection in a new global atmospheric dynamical core, HOMAM. The spatial discretization of the model is based on the discontinuous Galerkin method, combining the 2D horizontal elements on the cubed-sphere surface and 1D vertical elements in the terrain-following height-based coordinate. The time integrators are the horizontally explicit and vertically implicit (HEVI), split-explicit scheme HEVE and un-split third-order Runge-Kutta scheme. Two challenging advection tests from the DCMIP test suite were used for validating the schemes. The convergence shows a second-order accuracy with the smooth scalar field, irrespective of a particular time-integrator. For the non-smooth transport, the split schemes work well and results are comparable with other published results. Further rigorous testing of the time-splitting schemes with the nonhydrostatic HOMAM is in progress.

### Acknowledgments

The authors are thankful to Dr. David Hall for discussing the results with the CAM-SE model. RDN would like to thank KIAPS, Seoul, South Korea for the support.

## References

- [1] L. Bao, R. Klöforn, and R. D. Nair. Horizontally explicit and vertically implicit (HEVI) time discretization scheme for a discontinuous Galerkin nonhydrostatic model. *Mon. Wea. Rev.*, 2015. DOI:10.1175/MWR-D-14-00083.1.

- [2] S. Brdar, M. Baldauf, A. Dedner, and R. Klöforn. Comparison of dynamical cores for NWP models: comparison of COSMO and Dune. *Theor. Comput. Fluid Dyn.*, 27:453–472, 2013.
- [3] T. L. Clark. A small-scale dynamics model using a terrain-following coordinate transformation. *J. Comput. Phys.*, 24:186–215, 1977.
- [4] B. Cockburn. An introduction to the Discontinuous-Galerkin method for convection-dominated problems. In A. Quarteroni, editor, *Lecture Notes in Mathematics: Advanced Numerical Approximation of Nonlinear Hyperbolic Equations*, volume 1697, pages 151–268. Springer, 1997.
- [5] J. M. Dennis, J. Edwards, K. J. Evans, O. Guba, P. H. Lauritzen, A. A. Martin, A. St-Cyr, M. A. Taylor, and P. H. Worely. CAM-SE: a scalable spectral element dynamical core for the community atmosphere model. *International Journal of High Performance Computing Applications*, 26:74–89, 2012.
- [6] T. Gal-Chen and R. C. Somerville. On the use of a coordinate transformation for the solution of navier-stokes. *J. Comput. Phys.*, 17:209–228, 1975.
- [7] S. Gottlieb, C.-W. Shu, and E. Tadmor. Strong Stability-Preserving high-order time discretization methods. *SIAM Review*, 43(1):89–112, 2001.
- [8] D. Hall, M. Taylor, P. Ullrich, K. Reed, C. Jablonowski, R. Nair, and H. Tufo. Dynamical core model intercomparison project: CAM-SE passive tracer transport. *Q. J. Roy. Meteor. Soc.*, 000:000–000, 2015.
- [9] C. Jablonowski, P. A. Ullrich, J. Kent, K. A. Reed, M. A. Taylor, P. H. Lauritzen, and R. D. Nair. *The 2012 Dynamical Core Model Intercomparison Project*, <https://www.earthsystemcog.org/projects/dcmip-2012/>, 2012.
- [10] J. F. Kelley and F. X. Giraldo. A continuous and discontinuous Galerkin methods for a scalable three-dimensional nonhydrostatic atmospheric model: Limited-area mode. *J. of Comput. Phys.*, 231:7988–8008, 2012.
- [11] J. Kent, P. A. Ullrich, and C. Jablonowski. Dynamical core model intercomparison project: Tracer transport test cases. *Q. J. Roy. Meteor. Soc.*, 140:1279–1293, 2014.
- [12] R. D. Nair, H.-W. Choi, and H. M. Tufo. Computational aspects of a scalable high-order Discontinuous Galerkin atmospheric dynamical core. *Computers and Fluids*, 38:309–319, 2009.
- [13] R. D. Nair, M. N. Levy, and P. H. Lauritzen. Emerging numerical methods for atmospheric modeling. In P. H. Lauritzen, C. Jablonowski, M. A. Taylor, and R. D. Nair, editors, *Numerical Techniques for Global Atmospheric Models*, volume 80, pages 189–250. Springer-Verlag, 2011. LNCSE.
- [14] R. D. Nair, S. J. Thomas, and R. D. Loft. A Discontinuous Galerkin transport scheme on the cubed sphere. *Mon. Wea. Rev.*, 133:814–828, 2005.
- [15] J. Simmaro and M. Hortal. A semi-implicit non-hydrostatic dynamical kernel using finite elements in the vertical discretization. *Q. J. R. Meteorol. Soc.*, 138:826–839, 2012.
- [16] W. C. Skamarock, J. B. Klemp, M. G. Duda, L. D. Flower, S-H. Park, and T. D. Ringler. A multi-scale nonhydrostatic atmospheric model using centroidal voronoi tessellations and c-grid staggering. *Mon. Wea. Rev.*, 140:3090–3105, 2012.
- [17] H. Tomita, K. Goto, and M. Satoh. A new approach to atmospheric general circulation model: Global cloud resolving model NICAM and its computational performance. *SIAM J. Sci. Comput.*, 30:2755–2776, 2008.
- [18] P. Ullrich and C. Jablonowski. A nonhydrostatic atmospheric dynamical core utilizing high-order finite-volume methods. *J. Comp. Phys.*, 231:5078–5108, 2012.
- [19] G. Zagal, D. Reinert P. Ripodas, and M. Baldauf. The ICON (icosahedral non-hydrostatic) modelling framework of DWD and MPI-M: Description of the non-hydrostatic dynamical core. *Q. J. R. Meteorol. Soc.*, pages 1–17, 2014. DOI: 10.1002/qj.2378.